Photocatalytic performance of PMN-PT@TiO₂ highly enhanced by alternative spatial electric field induced charge separation effect

Baoying Dai [a, b, c], Chunhua Lu [a, b, c, *], Jiahui Kou [a, b, c, **], Zhongzi Xu [a, b, c], Fulei Wang [d]

[a] State Key Laboratory of Materials-Oriented Chemical Engineering, College of Materials Science and Engineering, Nanjing Tech University, Nanjing, 210009, PR China
[b] Jiangsu Collaborative Innovation Center for Advanced Inorganic Function Composites, Nanjing Tech University, Nanjing, 210009, PR China
[c] Jiangsu National Synergetic Innovation Center for Advanced Materials (SICAM), Nanjing Tech University, Nanjing, 210009, PR China
[d] State Key Laboratory of Crystal Materials, Shandong University, Jinan, 250100, PR China

ABSTRACT

Efficient charge separation is a vital factor to gain high photocatalytic activity. Alternative spatial electric field generated by piezoelectric effect could significantly accelerate charge separation when introduced into photocatalyst system. In this work, famous piezoelectric lead magnesium niobate-lead titanate $0.675Pb(Mg_{1/3}Nb_{2/3})O_3$-$0.325PbTiO_3$ (PMN-PT) was firstly constructed with TiO₂ to prepare composite photocatalyst PMN-PT@TiO₂. The results indicate that the alternative spatial electric field, excited by ultrasonic wave vibration, greatly improves the photocatalytic degradation efficiency of rhodamine B (RhB) over PMN-PT@TiO₂ by about 50%. The durability experiments suggest that PMN-PT@TiO₂ can keep excellent photocatalytic stability even after several runs. Moreover, in the photocatalytic degradation of methylene blue (MB), the enhancement effect of alternative spatial electric field on photocatalytic performance is also observed. Importantly, this study provides a general method for constructing piezoelectric-based photocatalyst to capture solar energy, acoustic wave energy and wind energy, which will realize multi-field energy coupling and high photocatalysis.

© 2016 Elsevier B.V. All rights reserved.

1. Introduction

Photocatalysis technology utilizing solar energy has been considered a promising avenue to solve the current energy and environmental problems, which attracts more and more attentions [1–5]. Up to now, a vast number of photocatalysts have been employed to purify environment over the past decades, such as TiO₂, ZnO, WO₃, BiVO₄ and g-C₃N₄ [6–19]. Efficient charge separation is an imperative requirement to gain high photocatalytic activity, many modification methods have been proposed in terms of charge separation to further improve the photocatalytic activity, including the preparation of heterojunction, depositing noble metal and introducing extra electric field [20–28], but the

photocatalytic performance is not good enough for the practical application. So it is still a big challenge to explore efficient strategies for high photocatalytic performance.

Recently, Wang, et al. introduced piezoelectric-based spatial electric field by mechanical energy, ultrasonic wave vibration and thermal stress to enhance photocatalytic property, which is possibly due to the promotion effect on charge separation. It aroused wide interest from the view of both theory and practical application [1,29,30]. It was mentioned that the higher piezoelectric effect is helpful for the improvement of photocatalytic activity [30]. However, in the previous work, ZnO and BaTiO₃ were selected to generate piezoelectric-based spatial electric field, and their low piezoelectric effect resulted in poor charge separation effect and limited their enhancement on the photocatalysis. Therefore, the materials possessing excellent piezoelectric effect should be investigated to construct photocatalysts with high photocatalytic performance.

Lead magnesium niobate-lead titanate $(1-x)Pb(Mg_{1/3}Nb_{2/3})O_3$-$xPbTiO_3$ ((1-x)PMN-xPT), a promising new generated piezoelectric material, exhibits a brilliant piezoelectric coupling coefficient (d_{33}) up to 2500 pm/V [31–33], which is much higher than that of

conventional ceramics. For example, the piezoelectric coupling coefficient (d_{33}) of single crystal bulk (1-x)PMN-xPT is almost 30 times higher than that of $BaTiO_3$ bulk material, and even 90 times higher than that of ZnO [34,35]. When the molecular proportion of $PbTiO_3$ in (1-x)PMN-xPT is between 32% and 35%, the rhombohedral-tetragonal morphotropic phase boundary (MPB) of (1-x)PMN-xPT is formed, which provides the material with superior piezoelectric property [36]. $0.675Pb(Mg_{1/3}Nb_{2/3})O_3$-$0.325PbTiO_3$ (PMN-PT) is reported to be one of the best piezoelectric materials among all the (1-x)PMN-xPT system [37]. Hence, the introduction of PMN-PT into photocatalyst system is needed. Moreover, the systemically study has important realistic significance for developing the role of spatial electric field in photocatalysis.

In this work, to reveal the effect of alternative spatial electric field on photocatalysis and develop high performance photocatalyst, piezoelectric PMN-PT was firstly used to fabricate novel composite photocatalyst PMN-PT@TiO$_2$. The photocatalytic degradations of RhB and MB were studied in the presence and absence of alternative spatial electric field, respectively. The piezoelectric property of blank PMN-PT particles was investigated by PFM, and the piezoelectric potential output of PMN-PT was simulated with COMSOL multiphysics software. The photocatalytic stabilities of PMN-PT and PMN-PT@TiO$_2$ were investigated for several runs.

2. Experimental

2.1. Materials

All the reagents were of analytical grade and were used without future purification. Distilled water was used in the whole experiment. Magnesium carbonate basic pentahydrate (($MgCO_3)_4 \cdot Mg(OH)_2 \cdot 5H_2O$, 40.0–44.5%), niobium (V) oxide (Nb_2O_5, 99.5%), trilead tetraoxide (Pb_3O_4, 95.0%), titanium dioxide (TiO_2, 98.0%) and ethanol (CH_3CH_2OH, 99.7%) were purchased from Sinopharm Chemical Reagent Co., Ltd. To synthesize nano titanium dioxide (TiO_2) powders, tetrabutyl titanate ($Ti(OC_4H_9)_4$, 98.0%) was purchased from Shanghai Lingfeng Chemical Reagent Co., Ltd.

2.2. Preparations

TiO_2 nanoparticles were synthesized through a reported hydrothermal method [38]. 7 mL ethanol was mixed with 61 mL distilled water by magnetic stirring for 10 min, and then 8 mL tetrabutyl titanate was added dropwise into the solution. After continuously stirred for 30 min, the final mixture was transferred into a 100 mL homemade polytetrafluoroethylene lined stainless steel reactor. Hydrothermal reaction was conducted at 150 °C for 24 h. After cooling down to room temperature, the reaction product was centrifuged and washed with distilled water and ethanol for several times, then the precipitates were dried at 60 °C overnight in an oven.

PMN-PT powders were prepared by a two-stage solid phase sintering method [37]. Magnesium niobate ($MgNb_2O_6$) was synthesized at the first stage. To obtain stoichiometric proportion magnesium niobate, magnesium carbonate basic pentahydrate (treated as MgO) and niobium (V) oxide with a molar ratio of 1.02 were mixed in ethanol for 24 h by planetary ball milling. After the mixture was dried and ground, the obtained powders were sintered at 1000 °C for 2 h. The second stage was to prepare PMN-PT. The mixture of magnesium niobate, trilead tetraoxide and titanium dioxide with the molar ratio of 0.225:0.337:0.325 was milled for 24 h in ethanol and dried over night to get well-proportioned reaction powders. Then the powders were pre-sintered at 700 °C for 0.5 h, and sintered at 800 °C for 3 h during the second sintering

process. At last, the obtained product was ground and sieved through 200 mesh before utilized.

The method to fabricate PMN-PT@TiO$_2$ was similar to the synthesis process of TiO$_2$. At first, 10.0 g of as-prepared lead magnesium niobate-lead titanate powders were ultrasonic dispersed in the solution consisted of 61 mL distilled water and 7 mL ethanol for 10 min. Secondly, 8 mL of tetrabutyl titanate was added in drops and the final mixture was vigorously stirred for 30 min. Thirdly, the reaction mixture was poured into a 100 mL homemade polytetrafluoroethylene lined stainless steel reactor and aged at 150 °C for 24 h. After cooling down to room temperature, the product was isolated by centrifugation, washed with distilled water and ethanol for several times, and dried overnight in an oven. Finally, the prepared powders were ground and sieved through 200 mesh.

2.3. Characterizations

The structure characterization of as-prepared samples was performed on a SmartLab (Rigaku) thin-film diffractometer employing Cu K$_\alpha$ radiation ($\lambda = 0.15406$ nm), with a scanning rate of 10°/min in the 2θ angle ranged from 20° to 70°. Scanning electron microscopy (SEM) was performed with a S-4800 scanning electron analyzer with an accelerating voltage of 15 kV. High resolution transmission electron microscopy (HRTEM) images were acquired with a 200 kV FEI Tecnai. UV−vis diffuse reflection spectra were obtained for the as-prepared samples using an ultraviolet−visible−near infrared (UV−Vis-Nir) 3101 spectrophotometer (Shimadzu) with $BaSO_4$ as the reflectance sample in the wavelength ranged from 200 to 800 nm. The absorption spectra were converted from reflection by the Kubelka-Munk method. PFM was performed using a Bruker Dimension Icon Scanning Probe Microscope with a Pt-coated conductive tip. A 10 V AC voltage was applied on the conductive tip of the PFM to detect the piezoelectric response of PMN-PT particles.

A 15 W lamp ($\lambda_{max} = 254$ nm) was used as UV light source, which irradiated at a distance of 20 cm to the reacting substance. The ultrasonic wave was introduced by a SK3300HP ultrasonic machine (Kedao) with the working frequency of 53 kHz and the consumed power of 180 W. The degradation efficiency of commercial organic dye RhB (12 mg/L, 50 mL) over prepared samples were studied under ultrasonic wave vibration in the presence (U-L) and absence (U-NL) of UV light irradiation, as a contrast, the photocatalytic reactions were also carried out using magnetic stirring under UV light illumination (S-L). Prior to catalytic reaction, 50 mg powders were ultrasonic dispersed in 30 mL distilled water for 1 h to avoid the agglomeration of the particles, and then 20 mL 30 mg/L RhB was added to form a 12 mg/L organic dye solution. After that, the suspension was stirred for 1 h in the dark to establish absorption-desorption equilibrium. The degradation experiments of MB (6 mg/L, 50 mL) over PMN-PT@TiO$_2$ were conducted similar to that of RhB. During all the catalytic process, any temperature rises caused by ultrasonic wave vibration, magnetic stirring and/or UV light irradiation were avoided by cool alcohol circulation. During the testing process, 3 mL of the sample solution was taken out every 30 min and analyzed by a UV−Vis-Nir 3101 spectrophotometer. The dye concentrations of RhB and MB were measured at its maximum absorption peak ($\lambda = 553$ nm for RhB and $\lambda = 664$ nm for MB), respectively. The percentage of degradation is designated as C/C_0 (C and C_0 are the test and original concentration of the measured dye solution, respectively). The durability experiments of RhB catalyzed by PMN-PT and PMN-PT@TiO$_2$ were carried out under UV light irradiation in the presence of ultrasonic wave vibration. After the suspension was measured, the photocatalyst powders were collected for the next run utilization.

3. Results and discussion

XRD, SEM and TEM were used to study the structures of the as-prepared samples. Fig. 1 shows the XRD patterns of TiO_2, PMN-PT and PMN-PT@TiO_2. The peaks of PMN-PT display that the fabricated sample is pure perovskite structured PMN-PT with the lattice constants of a = 4.03 Å, b = 4.00 Å, and c = 4.02 Å, which are consistent with the standard values of thin film PMN-PT [32,34]. All the diffraction peaks of TiO_2 can be found at 25.4°, 38.0°, 48.1°, 54.8° and 62.9°, which indicate the anatase structure of the sample [38,39]. The XRD patterns of composite PMN-PT@TiO_2 include all the diffraction peaks of PMN-PT and TiO_2 without any impurity peak. The result confirms that the original crystal structures of
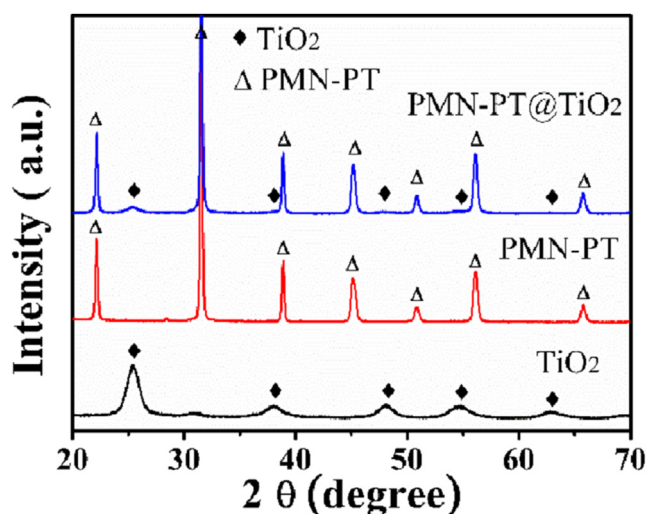
PMN-PT and TiO_2 are not changed through hydrothermal procedure.

The typical morphologies of PMN-PT, TiO_2 and PMN-PT@TiO_2 are depicted in Fig. 2. PMN-PT is composed of cubes with smooth surface, which are less than 1 μm (Fig. 2 (a)). Fig. 2 (b) suggests that TiO_2 synthesized through hydrothermal method are nano spherical particles. After being deposited by the small particles which are testified to be TiO_2 by HRTEM analysis (Fig. 2 (f)), the surface of PMN-PT@TiO_2 becomes rough, as Fig. 2 (c) displays. The TEM images (Fig. 2 (d) and (e)) of PMN-PT@TiO_2 indicate that the spherical TiO_2 nanoparticles are tightly and uniformly deposited on the surface of PMN-PT cubes. The diameter of TiO_2 particle is demonstrated to be almost the same, about 10 nm. The HRTEM image suggests that the interfaces of PMN-PT and TiO_2 contact compactly, indicating the formation of heterojunction between the interfaces of PMN-PT and TiO_2 particles. Moreover, the HRTEM image illustrates that the interplanar distances in the TiO_2 and PMN-PT portions are ca. 0.35 and 0.27 nm, corresponding to the spacing of the (101) and (110) planes of TiO_2 and PMN-PT, respectively.

UV−vis diffuse reflection spectra of as-prepared PMN-PT, TiO_2 and PMN-PT@TiO_2 powders were detected and converted to absorption spectra to study their optical absorption ability. As presented in Fig. 3 (a), the UV−vis absorption edges of TiO_2, PMN-PT and PMN-PT@TiO_2 are around 400 nm, 425 nm and 420 nm, respectively. From the onset of the absorption edge, the optical band gap is estimated by the following equation [40],

$$\alpha h\nu = A(h\nu - E_g)^n$$

in which α, h, ν, A and E_g are absorption coefficient, Plank constant, light frequency, proportional constant and band gap, respectively. In the equation, n depends on the characteristics of the transition in the semiconductor photocatalyst. The value of n for both TiO_2 and PMN-PT is determined as 2 (Fig. 3 (b)). The band gaps of TiO_2 and PMN-PT are determined to be about 2.95 and 2.62 eV, respectively.

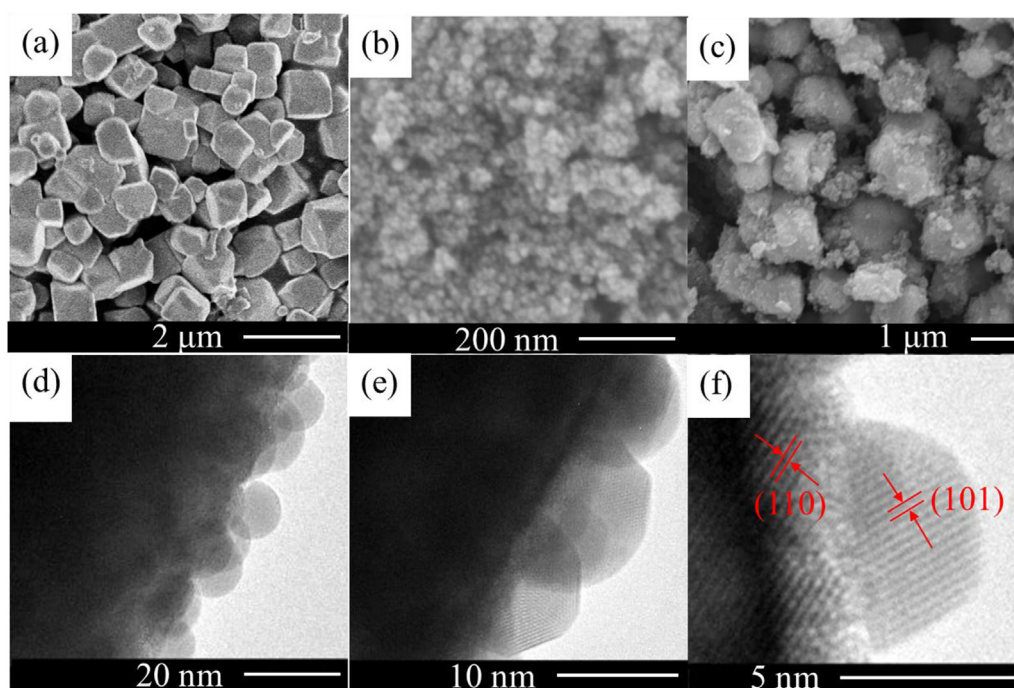Piezoelectric force microscopy is an effective technique to study

Fig. 1. XRD patterns of perovskite structured PMN-PT, anatase structured TiO_2 and composite PMN-PT@TiO_2.

Fig. 2. SEM images of (a) PMN-PT cubes, (b) TiO_2 particles and (c) composite PMN-PT@TiO_2 sample, (d, e) TEM images of PMN-PT@TiO_2 with different magnification, (f) HRTEM image of PMN-PT@TiO_2.
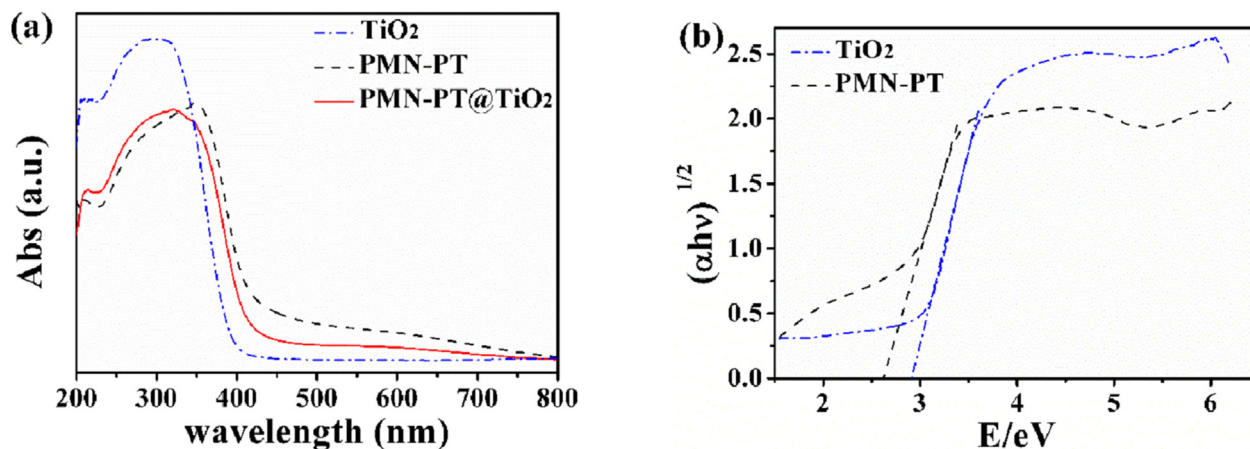
Fig. 3. (a) The UV—vis absorption spectra of prepared PMN-PT, TiO$_2$ and PMN-PT@TiO$_2$ powders, (b) the calculation diagram of PMN-PT and TiO$_2$ band gap.

the ferroelectric and piezoelectric phenomena in low dimensional materials [41—43], and it is therefore used to characterize the piezoelectric responses of PMN-PT powders. The piezoresponse magnitude can be estimated from the amplitude image of Fig. 4 (a). It demonstrates that PMN-PT particles possess piezoelectric property. The phase image is described in Fig. 4 (b), the dark and bright regions in particles are corresponding to the domains oriented upwards and backwards directions, respectively. The existence of 180° domains reveals that the PMN-PT sample is ferroelectric at room temperature. Moreover, it can be expected that the piezoelectric potential output will be detected if external force is acted on PMN-PT powders.

The photocatalytic capability of as-prepared samples for RhB degradation is presented in Fig. 5. The role of ultrasonic wave vibration in the photocatalytic performance was studied in the presence (Fig. 5 (a)) and absence (Fig. 5 (b)) of UV light irradiation. Fig. 5 (a) suggests that with the synergistic effect of ultrasonic wave vibration and UV light irradiation, the photocatalytic activity of the PMN-PT@TiO$_2$ sample is the highest, > 99%, while the conversions of RhB are 85% and 75% over TiO$_2$ and PMN-PT, respectively. As Fig. 5 (b) depicts, in the absence of light, the degradation rate of RhB on TiO$_2$ is similar with its self-degradation one under ultrasonic wave irradiation. PMN-PT and PMN-PT@TiO$_2$ induce a slight degradation of 15% and 18%, respectively, possibly caused by electrocatalytic mechanism [30]. As a contrast, the photocatalytic

reaction was also carried out using magnetic stirring under UV light irradiation (Fig. 5 (c)), displaying that the photocatalytic activity of TiO$_2$ is the highest, which is up to 75%, while the decolourization efficiencies of RhB over PMN-PT and PMN-PT@TiO$_2$ are just about 40% and 50%, respectively. The result reveals that the formation of heterojunction between the interfaces of PMN-PT and TiO$_2$ does not provide PMN-PT@TiO$_2$ with higher photocatalytic activity by using traditional magnetic stirring. To better compare the photocatalytic activity of prepared samples under the above three conditions, the degradation efficiencies of RhB at 210 min catalyzed by TiO$_2$, PMN-PT and PMN-PT@TiO$_2$ powders are summarized in Fig. 5 (d). Under the condition of U-L, the photocatalytic efficiency of PMN-PT@TiO$_2$ is the highest, while the efficiency of TiO$_2$ is the highest under the condition of S-L. Moreover, compared with magnetic stirring, the ultrasonic wave vibration improves the photocatalytic efficiency of PMN-PT@TiO$_2$, PMN-PT and TiO$_2$ by about 50%, 35% and 10% in the presence of UV light illumination, respectively. It indicates that the enhancement role of ultrasonic wave vibration in the photocatalytic activity of the as-prepared samples is different. Furthermore, there is nearly no difference in the degradation of RhB over as-prepared samples under the condition of U-NL, suggesting that the ultrasonic wave vibration itself is not the reason for the different photocatalytic activity enhancement. Given the piezoelectric and ferroelectric properties of PMN-PT, it is necessary to investigate the micro interaction between PMN-PT particles and
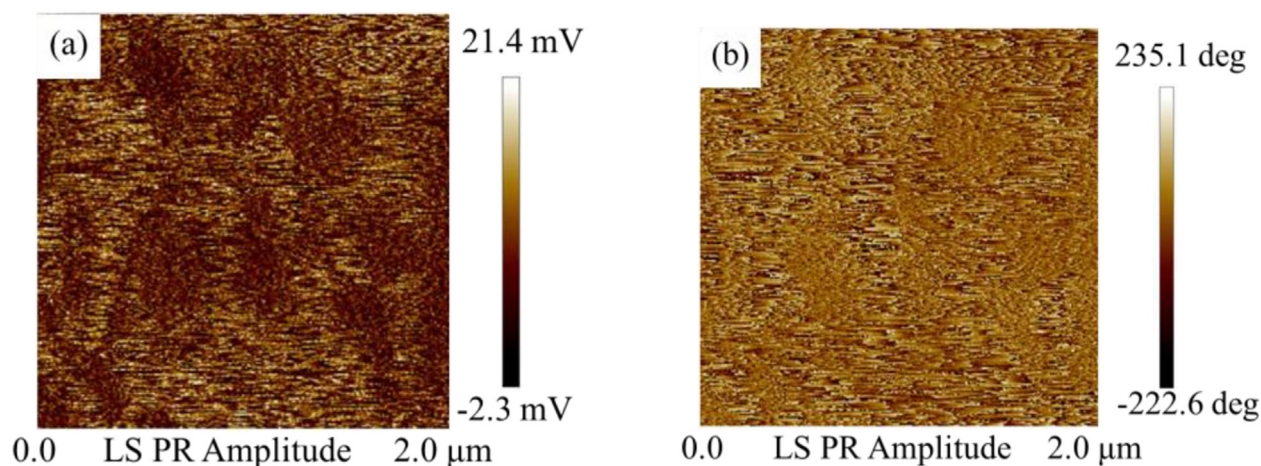

Fig. 4. PFM results of PMN-PT particles: (a) LS PR amplitude, (b) LS PR phase.
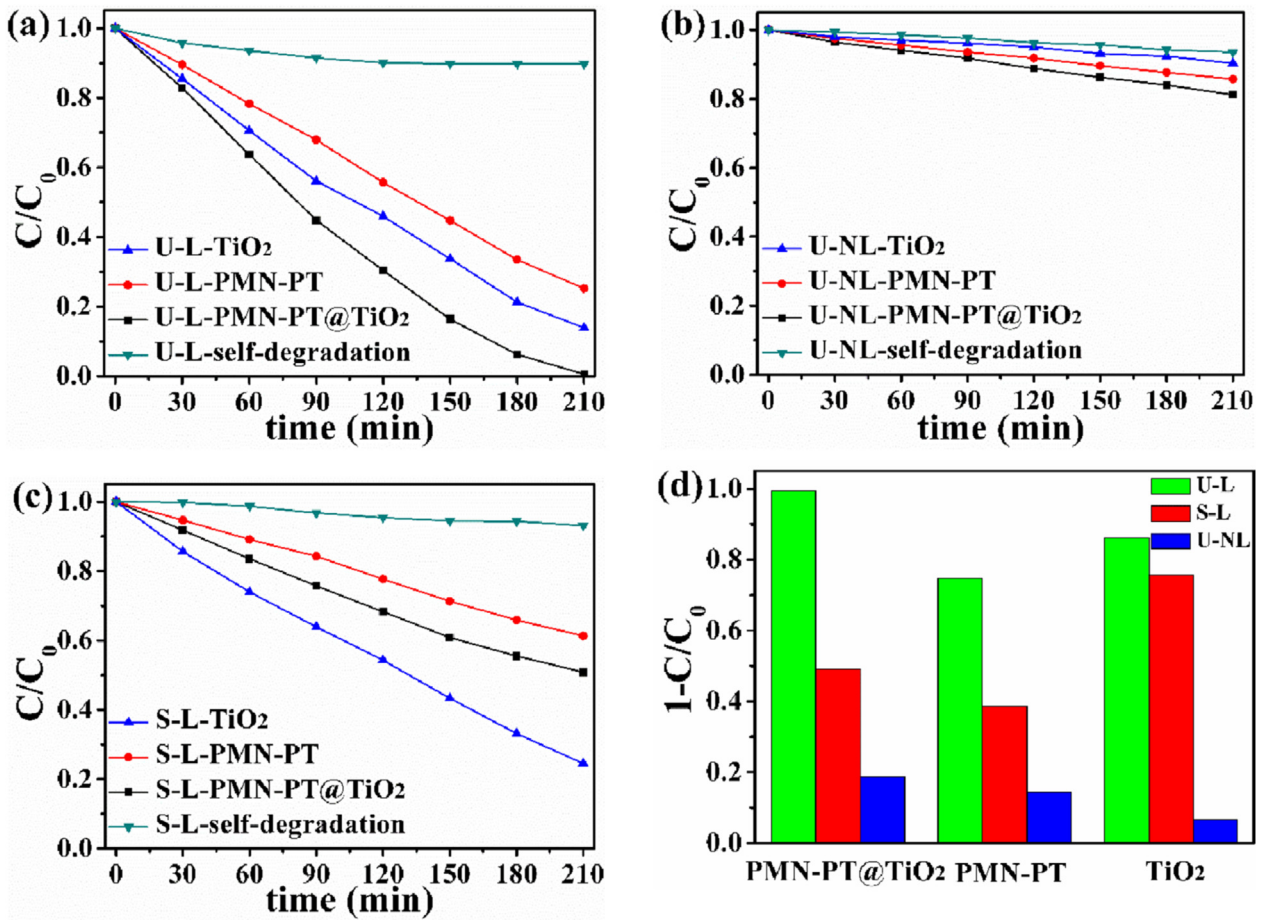
Fig. 5. The photocatalytic degradation patterns of RhB (12 mg/L, 50 mL) catalyzed by PMN-PT, TiO2 and PMN-PT@TiO2 under U-L (a), U-NL (b), and S-L (c). (d) Degradation efficiency of RhB at 210 min under the above mentioned three conditions.

ultrasonic wave vibration.

As we know, acoustic cavitation, an important phenomenon during ultrasonic wave vibration, could generate extremely active bubbles in water, which possess tremendous energy. It has been estimated from calculations that the pressure inside a water bubble can rise to more than 1000 atm [30,44]. The formation, growth and collapse of water bubbles in liquid medium are shown in Scheme 1. When piezoelectric PMN-PT powders are immersed in the water under ultrasonic wave vibration, the local high pressure, caused by the collapse of bubbles, will compel PMN-PT to deform periodically along with the vibration of ultrasonic wave, and the alternative spatial electric field generated by piezoelectric potential is formed simultaneously. Up to now, there is not an effective instrument to measure the deformation and piezoelectric potential of macro cubes under ultrasonic wave vibration. Therefore, the generated strain and piezoelectric potential of PMN-PT powders were simulated with COMSOL multiphysics software. The geometrical characteristics of the PMN-PT particles model were: width: 500 nm, depth: 500 nm, height: 500 nm (Fig. 6 (a1)). The bottom surface of the model was fixed and grounded, a 100 MPa (the pressure inside a water bubble) tensile (Fig. 6 (a2)) and compressive (Fig. 6 (a3)) stress were respectively applied to the upper surface along the negative z-axis. A shear stress (Fig. 6 (a4)), 100 MPa stress acting on the upper and left surface of PMN-PT along negative z-axis and x-axis simultaneously, was also introduced to simulate the deformation and piezoelectric potential of PMN-PT particles. The simulated maximum or minimum potential (Fig. 6 (b2), (b3) and (b4)) of PMN-PT results indicate that the generated potential outputs,

distributed on the surface of PMN-PT cube, are about 1.8, −1.8 and 3.5 V, respectively, which is big enough to accelerate the separation of photogenerated carriers.

With the synergistic of ultrasonic wave vibration and UV light irradiation, the interaction of photogenerated carriers and piezoelectric potential is illustrated in Scheme 2. In the presence of ultrasonic wave vibration, three types of piezoelectric potentials of PMN-PT (Scheme 2 (a)) and PMN-PT@TiO2 (Scheme 2 (b)) are randomly generated, and the corresponding alternative spatial electric field of PMN-PT is formed simultaneously. Hence, under UV light illumination, the photogenerated electrons (black spheres) and holes (white spheres) of PMN-PT (blue cubes), influenced by
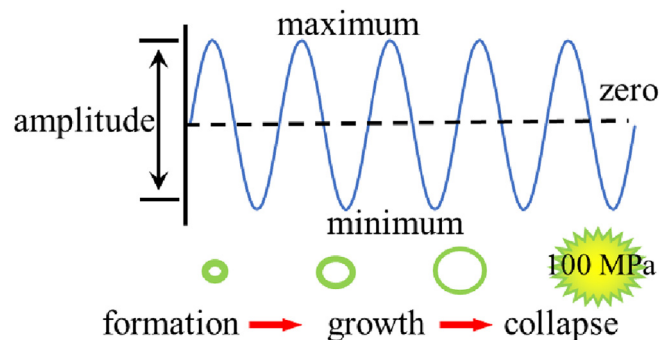
Scheme 1. Acoustic pressure vibration during sound wave propagation and cavitation phenomenon: formation, growth and collapse of bubbles in liquid medium [30].
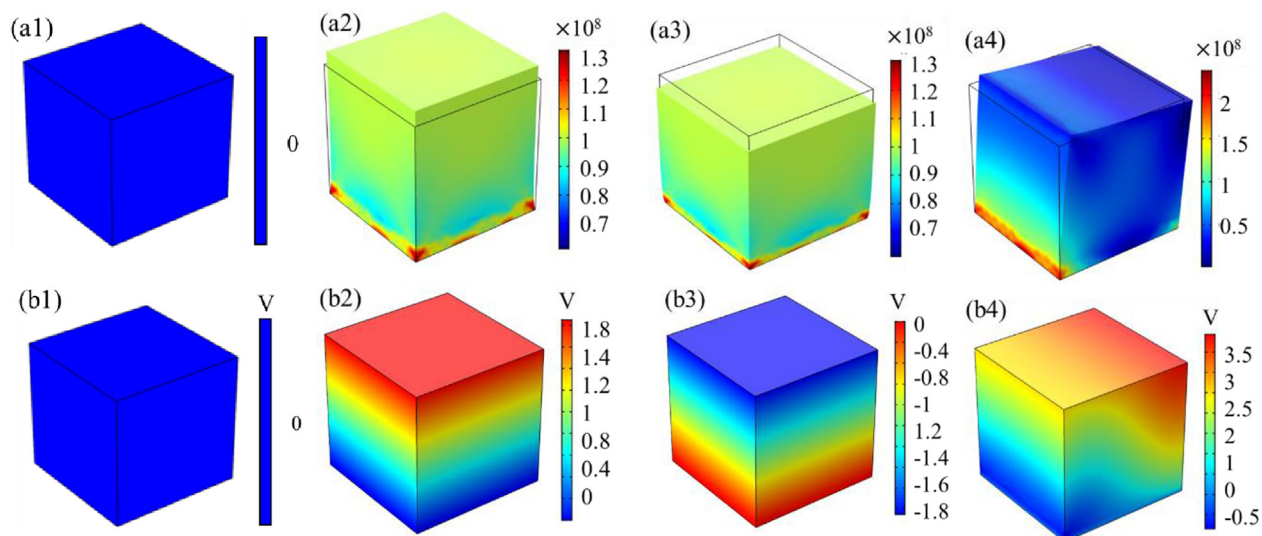
Fig. 6. Deformation of PMN-PT particles simulated with COMSOL multiphysics software under no stress (a1), tensile stress (a2), compressive stress (a3) and shear stress (a4), respectively, the corresponding piezoelectric potential outputs are displayed in (b1), (b2), (b3) and (b4).

the spatial electric field, will directionally transfer to the positive and negative potential surfaces, respectively. For the case of PMN-PT@TiO$_2$, the photogenerated electrons and holes of both PMN-PT (blue cubes) and TiO$_2$ (purple spheres) move simultaneously towards positive and negative potential surfaces of PMN-PT, respectively. Therefore, the separation of photogenerated carriers of PMN-PT and PMN-PT@TiO$_2$ is promoted during the catalytic process. It is worth noting that PMN-PT@TiO$_2$ possesses superior catalytic property than PMN-PT, as Fig. 5 (c) demonstrated, leading to an increase 50% in catalytic efficiency of PMN-PT@TiO$_2$ under U-L, which is much higher than that 35% of PMN-PT. Moreover, it is important to point out that a static electric field can be easily

saturated by photogenerated carriers [30], but the periodically alternative special electric field of PMN-PT cannot, suggesting that the role of special electric field in photocatalytic activity is played almost all the catalytic process, which makes the enhancement effect more sufficient.

The durability experiments of PMN-PT and PMN-PT@TiO$_2$ were carried out to estimate the stability of catalysts in the presence of ultrasonic wave vibration and UV light irradiation. As Fig. 7 describes, there is no obvious decrease in the catalytic efficiency of both PMN-PT and PMN-PT@TiO$_2$ even after five runs, suggesting the excellent stability of photocatalysts. The result demonstrates that the piezoelectric effect of PMN-PT doesn't get worse after UV
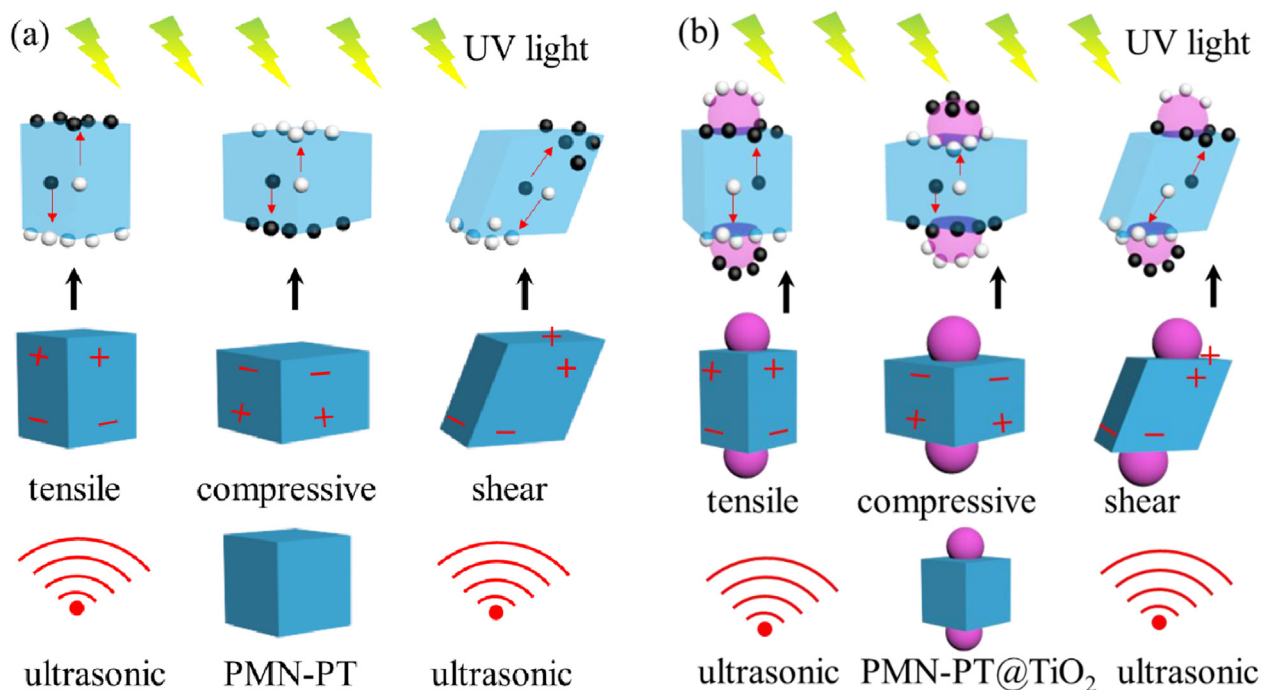
Scheme 2. The schematic details of the enhancement effect of spatial electric field introduced by ultrasonic wave vibration on the photocatalytic activity of PMN-PT (a) and PMN-PT@TiO$_2$ (b). The black, white, purple spheres and the blue cubes stand for photogenerated electrons, photogenerated holes, TiO$_2$ particles and PMN-PT cubes, respectively.
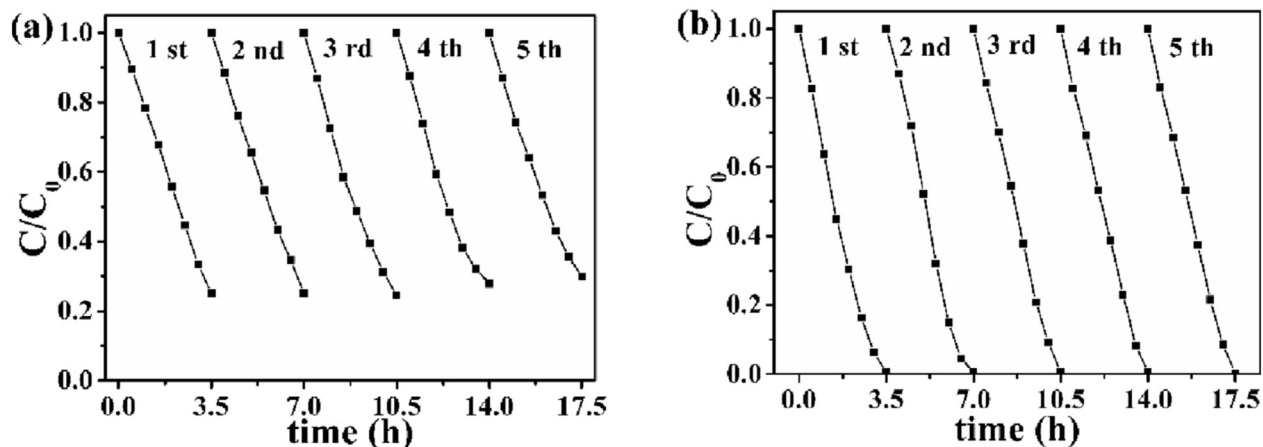
Fig. 7. The cyclic degradation curves of RhB (12 mg/L, 50 mL) solution catalyzed by PMN-PT (a) and PMN-PT@TiO$_2$ (b) under U-L.
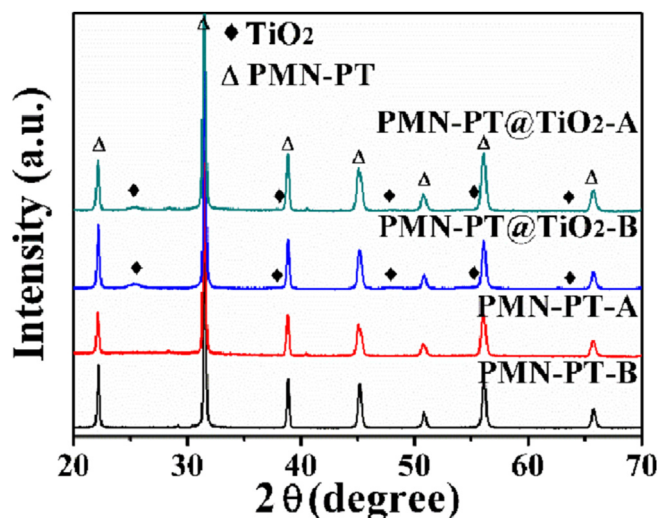

Fig. 8. XRD patterns of PMN-PT and PMN-PT@TiO$_2$ measured before and after durability experiments, letter A and B represent characterized after and before five runs, respectively.

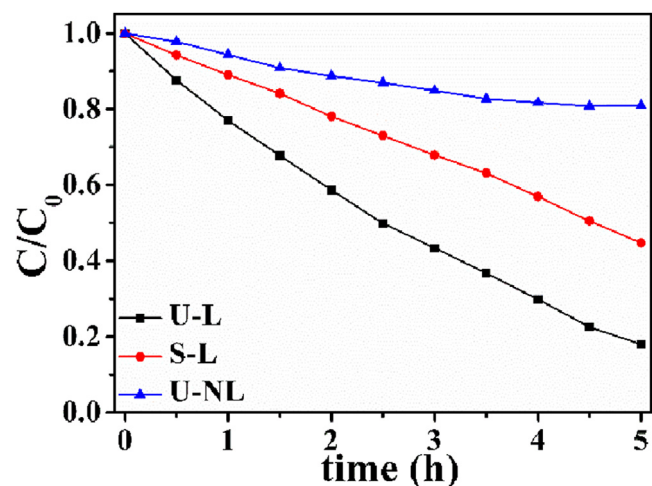**Fig. 9.** The degradation patterns of MB (6 mg/L, 50 mL) solution over PMN-PT@TiO$_2$ measured under U-L, S-L and U-NL, respectively.

light illumination and ultrasonic wave irradiation, and alternative spatial electric field steadily plays an enhancement role on photocatalytic activity throughout the five runs. The XRD patterns of PMN-PT and PMN-PT@TiO$_2$ characterized before and after durability experiments are depicted in Fig. 8. After five runs, all the diffraction peaks of PMN-PT@TiO$_2$ and PMN-PT remain the same as that characterized before, which indicates that the phases of both PMN-PT and PMN-PT@TiO$_2$ are not changed after long time UV light irradiation and ultrasonic wave vibration. It further manifests the brilliant stability of PMN-PT and PMN-PT@TiO$_2$.

The effect of alternative spatial electric field of PMN-PT on the photodegradation of MB over PMN-PT@TiO$_2$ was also investigated. Fig. 9 displays the degradation capability on MB solution measured in the presence and absence of UV light irradiation and ultrasonic wave vibration, as well as magnetic stirring and UV light illumination. Similar to the degradation situation of RhB, there is almost no degradation of MB under U-NL, and the degradation efficiency of MB is increased by about 25%, from 60% under S-L to 85% under U-L. The result demonstrates that the alternative spatial electric field is not only beneficial for the degradation of RhB, but also for that of MB.

4. Conclusions

In summary, we firstly constructed PMN-PT with TiO$_2$ to fabricate novel composite photocatalyst PMN-PT@TiO$_2$. With the assistant of the ultrasonic wave exited alternative spatial electric field of PMN-PT, the photodegradation capabilities on RhB and MB over PMN-PT@TiO$_2$ were highly improved by about 50% and 25%, respectively. The PFM images and the COMSOL multiphysics simulation results of PMN-PT sample verified its excellent piezoelectric property. The durability experiments and the XRD results of PMN-PT and PMN-PT@TiO$_2$ also demonstrated their good photocatalytic stabilities over five runs. Importantly, this study provides a general method for constructing various piezoelectric-based photocatalyst materials which will capture solar energy, acoustic wave energy and wind energy from nature to realize multi-field energy coupling and high photocatalysis. Hence, the enhancement effect of alternative spatial electric field on photocatalytic activity should be further studied and utilized in the practical application.

References

[1] X. Xue, W. Zang, P. Deng, Q. Wang, L. Xing, Y. Zhang, Z.L. Wang, Piezo-potential enhanced photocatalytic degradation of organic dye using ZnO nanowires, Nano Energy 13 (2015) 414–422.

[2] X. Jin, L. Ye, H. Wang, Y. Su, H. Xie, Z. Zhong, H. Zhang, Bismuth-rich strategy induced photocatalytic molecular oxygen activation properties of bismuth oxyhalogen: the case of Bi24O31Cl10, Appl. Catal. B Environ. 165 (2015) 668–675.

[3] W. Wang, M.O. Tade, Z. Shao, Research progress of perovskite materials in photocatalysis- and photovoltaics-related energy conversion and environmental treatment, Chem. Soc. Rev. 44 (2015) 5371–5408.

[4] H. Li, T. Hu, N. Du, R. Zhang, J. Liu, W. Hou, Wavelength-dependent differences in photocatalytic performance between BiOBr nanosheets with dominant exposed (001) and (010) facets, Appl. Catal. B Environ. 187 (2016) 342–349.

[5] H. Heng, Q. Gan, P. Meng, X. Liu, The visible-light-driven type III heterojunction H3PW12O40/TiO2-In2S3: a photocatalysis composite with enhanced photocatalytic activity, J. Alloys Compd. 696 (2017) 51–59.

[6] C. Liu, L. Zhang, R. Liu, Z. Gao, X. Yang, Z. Tu, F. Yang, Z. Ye, L. Cui, C. Xu, Y. Li, Hydrothermal synthesis of N-doped TiO2 nanowires and N-doped graphene heterostructures with enhanced photocatalytic properties, J. Alloys Compd. 656 (2016) 24–32.

[7] L. Liu, C. Luo, J. Xiong, Z. Yang, Y. Zhang, Y. Cai, H. Gu, Reduced graphene oxide (rGO) decorated TiO2 microspheres for visible-light photocatalytic reduction of Cr(VI), J. Alloys Compd. 690 (2017) 771–776.

[8] H.M. Yadav, J. Kim, Solvothermal synthesis of anatase TiO2-graphene oxide nanocomposites and their photocatalytic performance, J. Alloys Compd. 688 (2016) 123–129.

[9] F. Peng, Y. Ni, Q. Zhou, J. Kou, C. Lu, Z. Xu, Construction of ZnO nanosheet arrays within BiVO4 particles on a conductive magnetically driven cilia film with enhanced visible photocatalytic activity, J. Alloys Compd. 690 (2017) 953–960.

[10] A. Tayyebi, M. Outokesh, M. Tayebi, A. Shafikhani, S.S. Şengör, ZnO quantum dots-graphene composites: formation mechanism and enhanced photocatalytic activity for degradation of methyl orange dye, J. Alloys Compd. 663 (2016) 738–749.

[11] M. Mansournia, L. Ghaderi, CuO@ZnO core-shell nanocomposites: novel hydrothermal synthesis and enhancement in photocatalytic property, J. Alloys Compd. 691 (2017) 171–177.

[12] S. Yao, X. Zhang, F. Qu, A. Umar, X. Wu, Hierarchical WO3 nanostructures assembled by nanosheets and their applications in wastewater purification, J. Alloys Compd. 689 (2016) 570–574.

[13] H. Xu, L. Liu, Y. Song, L. Huang, Y. Li, Z. Chen, Q. Zhang, H. Li, BN nanosheets modified WO3 photocatalysts for enhancing photocatalytic properties under visible light irradiation, J. Alloys Compd. 660 (2016) 48–54.

[14] M. Xie, Y. Feng, X. Fu, P. Luan, L. Jing, Phosphate-bridged TiO2-BiVO4 nanocomposites with exceptional visible activities for photocatalytic water splitting, J. Alloys Compd. 631 (2015) 120–124.

[15] C. Yu, S. Dong, J. Zhao, X. Han, J. Wang, J. Sun, Preparation and characterization of sphere-shaped BiVO4/reduced graphene oxide photocatalyst for an augmented natural sunlight photocatalytic activity, J. Alloys Compd. 677 (2016) 219–227.

[16] M. Ou, Q. Zhong, S. Zhang, L. Yu, Ultrasound assisted synthesis of heterogeneous g-C3N4/BiVO4 composites and their visible-light-induced photocatalytic oxidation of NO in gas phase, J. Alloys Compd. 626 (2015) 401–409.

[17] J. Jin, Q. Liang, C. Ding, Z. Li, S. Xu, Simultaneous synthesis-immobilization of Ag nanoparticles functionalized 2D g-C3N4 nanosheets with improved photocatalytic activity, J. Alloys Compd. 691 (2017) 763–771.

[18] Y. Kang, Y. Yang, L. Yin, X. Kang, G. Liu, H. Cheng, An amorphous carbon nitride photocatalyst with greatly extended visible-light-responsive range for photocatalytic hydrogen generation, Adv. Mater 27 (2015) 4572–4577.

[19] Q. Zhang, Z. Li, S. Wang, R. Li, X. Zhang, Z. Liang, H. Han, S. Liao, C. Li, Effect of redox cocatalysts location on photocatalytic overall water splitting over cubic NaTaO3 semiconductor crystals exposed with equivalent facets, Acs Catal. 6 (2016) 2182–2191.

[20] H. Li, Y. Zhou, W. Tu, J. Ye, Z. Zou, State-of-the-Art progress in diverse heterostructured photocatalysts toward promoting photocatalytic performance, Adv. Funct. Mater 25 (2015) 998–1013.

[21] M. Yan, Y. Hua, F. Zhu, W. Gu, J. Jiang, H. Shen, W. Shi, Fabrication of nitrogen doped graphene quantum dots-BiOI/MnNb2O6 p-n junction photocatalysts with enhanced visible light efficiency in photocatalytic degradation of antibiotics, Appl. Catal. B Environ. 202 (2017) 518–527.

[22] X. Wen, C. Zhang, C. Niu, L. Zhang, G. Zeng, X. Zhang, Highly enhanced visible light photocatalytic activity of CeO2 through fabricating a novel p–n junction BiOBr/CeO2, Catal. Commun. 90 (2017) 51–55.

[23] Y. Feng, C. Liu, J. Chen, H. Che, L. Xiao, W. Gu, W. Shi, Facile synthesis of BiOI/CdWO4 p-n junctions: enhanced photocatalytic activities and photoelectrochemistry, Rsc Adv. 6 (2016) 38290–38299.

[24] J.C. Matsubu, E.T. Lin, K.L. Gunther, K.N. Bozhilov, Y. Jiang, P. Christopher, Critical role of interfacial effects on the reactivity of semiconductor-cocatalyst junctions for photocatalytic oxygen evolution from water, Catal. Sci. Technol. 6 (2016) 6836–6844.

[25] L. Yu, L. Shao, D. Li, Direct combination of hydrogen evolution from water and methane conversion in a photocatalytic system over Pt/TiO2, Appl. Catal. B Environ. 204 (2017) 216–223.

[26] N. Güy, M. Özacar, The influence of noble metals on photocatalytic activity of ZnO for Congo red degradation, Int. J. Hydrogen Energ 41 (2016) 20100–20112.

[27] P. Zhang, X. Wu, T. Zhao, P. Hou, L. Wen, Influence of alternating current electric field on the photocatalytic activity of Mo6+-doped and Ag0-loaded nano-TiO2, J. Alloys Compd. 587 (2014) 511–514.

[28] Y. Xu, D. Zhong, J. Jia, K. Li, J. Li, X. Quan, Dual slant-placed electrodes thin-film photocatalytic reactor: enhanced dye degradation efficiency by self-generated electric field, Chem. Eng. J. 225 (2013) 138–143.

[29] L. Wang, S. Liu, Z. Wang, Y. Zhou, Y. Qin, Z.L. Wang, Piezotronic effect enhanced photocatalysis in strained anisotropic ZnO/TiO2 nanoplateletsvia thermal stress, Acs Nano 10 (2016) 2636–2643.

[30] H. Li, Y. Sang, S. Chang, X. Huang, Y. Zhang, R. Yang, H. Jiang, H. Liu, Z.L. Wang, Enhanced ferroelectric-nanocrystal-based hybrid photocatalysis by Ultrasonic-wave-generated piezophototronic effect, Nano Lett. 15 (2015) 2372–2379.

[31] S. Xu, G. Poirier, N. Yao, Fabrication and piezoelectric property of PMN-PT nanofibers, Nano Energy 1 (2012) 602–607.

[32] S. Xu, G. Poirier, N. Yao, PMN-pt nanowires with a very high piezoelectric constant, Nano Lett. 12 (2012) 2238–2242.

[33] C. Li, X. Liu, W. Luo, D. Xu, K. He, Surfactant-Assisted hydrothermal synthesis of PMN-PT nanorods, Nanoscale Res. Lett. 11 (2016).

[34] S. Xu, Y. Yeh, G. Poirier, M.C. McAlpine, R.A. Register, N. Yao, Flexible piezoelectric PMN-PT nanowire-based nanocomposite and device, Nano Lett. 13 (2013) 2393–2398.

[35] G. Hwang, H. Park, J. Lee, S. Oh, K. Park, M. Byun, H. Park, G. Ahn, C.K. Jeong, K. No, H. Kwon, S. Lee, B. Joung, K.J. Lee, Self-powered cardiac pacemaker enabled by flexible single crystalline PMN-PT piezoelectric energy harvester, Adv. Mater 26 (2014) 4880–4887.

[36] W.B. Luo, K. He, D. Xu, C. Li, X.Y. Bai, Y. Shuai, C.G. Wu, W.L. Zhang, Reactive temperature and growth time effects on the morphology of PMN-PT nanorods by hydrothermal synthesis, J. Alloys Compd. 671 (2016) 122–126.

[37] W. Shi, Grain-alignment Control Preparation of PMN-PT and BNT Piezoelectric Ceramics, Nanjing University of Technology, 2008.

[38] G. Wang, Hydrothermal synthesis and photocatalytic activity of nanocrystalline TiO2 powders in ethanol-water mixed solutions, J. Mol. Catal. A Chem. 274 (2007) 185–191.

[39] Y. Wei, J. Jiao, Z. Zhao, W. Zhong, J. Li, J. Liu, G. Jiang, A. Duan, 3D ordered macroporous TiO2-supported Pt@CdS core-shell nanoparticles: design, synthesis and efficient photocatalytic conversion of CO2 with water to methane, J. Mater. Chem. A 3 (2015) 11074–11085.

[40] J. Kou, H. Zhang, Z. Li, S. Ouyang, J. Ye, Z. Zou, Photooxidation of polycyclic aromatic hydrocarbons over NaBiO3 under visible light irradiation, Catal. Lett. 122 (2008) 131–137.

[41] H.L.Y.S. Shaozheng Ji, Synthesis, structure, and piezoelectric properties of ferroelectric and antiferroelectric NaNbO3 nanostructures, Crystengcomm 16 (2014) 7598–7604.

[42] D. Liu, C. Ma, H. Luo, Y. Tang, W. Shi, D. Sun, F. Wang, T. Wang, Nanoscale insight into the domain structures of high Curie point Pb(In1/2Nb1/2)O3-PbTiO3 single crystal, J. Alloys Compd. 696 (2017) 166–170.

[43] K.Y. Zhao, W. Zhao, H.R. Zeng, H.Z. Yu, W. Ruan, K.Q. Xu, G.R. Li, Tip-bias-induced domain evolution in PMN-PT transparent ceramics via piezoresponse force microscopy, Appl. Surf. Sci. 337 (2015) 125–129.

[44] E.B. Flint, K.S. Suslick, The temperature of cavitation,, Science 253 (1991) 1397–1399.